A dual-stage method for lesion segmentation on digital mammograms

Yading Yuan,[a] Maryellen L. Giger, Hui Li, Kenji Suzuki, and Charlene Sennett
Department of Radiology, Committee on Medical Physics, The University of Chicago,
5841 South Maryland Avenue-MC 2026, Chicago, Illinois 60637

Mass lesion segmentation on mammograms is a challenging task since mass lesions are usually embedded and hidden in varying densities of parenchymal tissue structures. In this article, we present a method for automatic delineation of lesion boundaries on digital mammograms. This method utilizes a geometric active contour model that minimizes an energy function based on the homogeneities inside and outside of the evolving contour. Prior to the application of the active contour model, a radial gradient index (RGI)-based segmentation method is applied to yield an initial contour closer to the lesion boundary location in a computationally efficient manner. Based on the initial segmentation, an automatic background estimation method is applied to identify the effective circumstance of the lesion, and a dynamic stopping criterion is implemented to terminate the contour evolution when it reaches the lesion boundary. By using a full-field digital mammography database with 739 images, we quantitatively compare the proposed algorithm with a conventional region-growing method and an RGI-based algorithm by use of the area overlap ratio between computer segmentation and manual segmentation by an expert radiologist. At an overlap threshold of 0.4, 85% of the images are correctly segmented with the proposed method, while only 69% and 73% of the images are correctly delineated by our previous developed region-growing and RGI methods, respectively. This resulting improvement in segmentation is statistically significant. © *2007 American Association of Physicists in Medicine*. [DOI: 10.1118/1.2790837]

Key words: Mass lesion segmentation, geometric active contour model, computer-aided diagnosis, breast cancer

I. INTRODUCTION

Breast cancer is the most common malignancy in American women and the second most common cause of death from malignancy in this population. According to the American Cancer Society, about 178,480 women in the United States will be found to have invasive breast cancer in 2007, and about 40,460 women will die from the disease this year.[1] Although some imaging modalities, such as magnetic resonance imaging (MRI)[2,3] and sonography,[4,5] are currently being investigated to improve sensitivity and specificity of breast cancer diagnosis, x-ray mammography is still the most prevalent imaging procedure for the early detection of breast cancer.

Lesion segmentation, which extracts the lesion from the surrounding tissues, is an essential step in the computerized analysis of mammograms. As mass lesions are usually embedded and hidden in varying densities of parenchymal structures, the task of lesion segmentation is not trivial. Many researchers have developed computer algorithms for this task. Huo *et al.*[6] employed a region-growing method to find the contour, in which abrupt changes in size and circularity were used as the rules of segmentation. Kupinski *et al.*[7] segmented the mass by applying either a radial gradient index (RGI) model or a probabilistic model to the lesion, multiplied by a constraint function. Petrick *et al.*[8] introduced a segmentation algorithm that combines a density-weighted contrast enhancement filter and a region growing method. Li *et al.*[9] employed a multiresolution Markov random field

model to detect tumors in mammographic images. Timp *et al.*[10] employed both edge based information as well as a priori knowledge about the gray level distribution of the region of interest (ROI) around the mass, and obtained an optimal contour using dynamic programming. To segment lesions, Guliato *et al.*[11] proposed two fuzzy sets related methods—one employing a region growing after fuzzy-sets-based preprocessing, and the other using a fuzzy region-growing method that takes into account the uncertainty present around the boundaries of tumor. Li *et al.*[12] presented a statistical model for enhanced segmentation and extraction of a suspicious mass area from mammographic images. In their study, a morphological operation is derived to enhance disease patterns of suspected masses by eliminating unrelated back-ground clutter, and a model-based image segmentation is performed to localize the suspected mass areas using stochastic relaxation labeling.

Originally introduced by Kass,[13] active contour models (or snakes) have attracted much attention as image segmentation techniques. An active contour model minimizes an energy functional along a deformable contour, which is influenced by both internal and external terms. The internal energy controls the smoothness and elasticity of the contour, while the external energy attracts the evolving contour to deform toward salient image features, such as edges. Although the active contour model has been used for segmenting objects in a wide range of medical applications,[14–19] to the best of our knowledge, few works have applied this

model to the task of lesion segmentation in mammographic images. Brake *et al.*[20] segmented mass lesions by a discrete active contour method, whose external energy was determined by the image gradient magnitude. Sahiner *et al.*[21] applied an active contour model that incorporated edge and region analysis, in which the contour energy was minimized by a greedy algorithm. In their work, however, the contour was represented by the vertices of an *N*-points polygon and each vertex was tracked during the process, which makes it difficult for the contour to adapt to a change of topology, such as splitting or merging parts.

Differing from the segmentation methods mentioned above, in this study we develop an automatic lesion segmentation algorithm that employs a geometric active contour model to extract lesions. Geometric active contour models[22,23] represent contours as a level set of a higher-dimensional scalar function.[24] The contours are obtained only after complete evolution, thereby allowing the model to handle the topological changes naturally. As mass lesions usually have weak edges, we use a region-based active contour model[25] that is based on global image information, and is less sensitive to noise and the initial contour. In order to improve the computational efficiency and suppress the influence of unrelated structures, our previous RGI-based segmentation method[7] is applied first to delineate an initial contour, which is relatively close to the actual margin, and to estimate the effective background. We then exploit a dynamic stopping criterion, which is solely based on the property of the given image, to terminate the evolving procedure automatically.

The organization of this paper is as follows: Section II introduces the database used for this study. Section III describes the proposed segmentation method. Section IV presents the results, and Sections V and VI give a discussion and conclusion, respectively.

II. MATERIALS

In this study, we used a full-field digital mammography (FFDM) database, which consists of 139 benign (327 mammograms) and 148 malignant (412 mammograms) lesions. All of the images were collected from the University of Chicago Hospitals and obtained from GE Senographe 2000D systems (GE Medical Systems, Milwaukee, WI) with a spatial resolution of $95~\mu m \times 95~\mu m$. The masses were identified and outlined by an expert breast radiologist based on visual criterion and biopsy-proven reports. These outlines were used as the "gold standard" for calibrating parameters and evaluating performance. The distributions of effective projection diameter, which is defined as the effective diameter of the area inside the radiologist's manually delineated contours, are shown in Fig. 1.

III. METHODS

The main aspects of the proposed segmentation method include an initial RGI segmentation,[7] background estimation
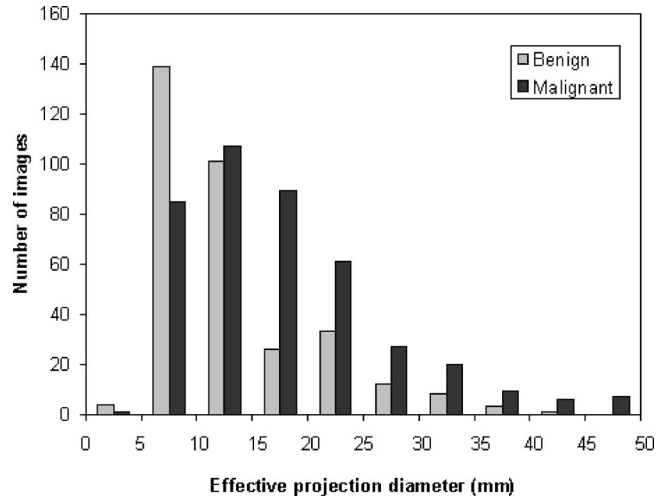

FIG. 1. Distribution of lesions' effective diameters obtained from the FFDM database.

and trend correction, and an active contour segmentation based on level sets. Figure 2 shows the flow chart of the overall implementation.

III.A. Active contour model

The active contour model[25] relies on an intrinsic property of image segmentation: For an image formed by two regions, each segmented region should be as homogeneous as possible. Mathematically, this model can be expressed by the following energy function:
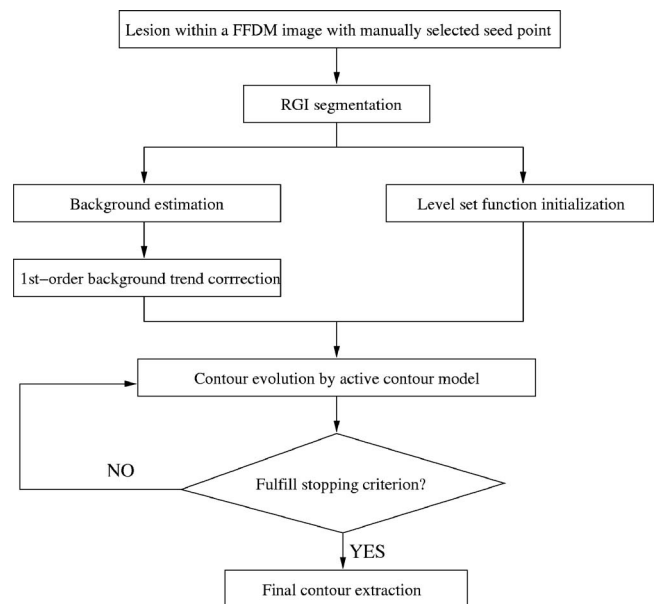

FIG. 2. Schematic diagram of the proposed dual-stage lesion segmentation algorithm.

$$E(c_1, c_2, C) = \mu \cdot \text{length}(C)$$

$$+ \lambda_1 \cdot \int_{\text{inside}(C)} |f_0(x,y) - c_1|^2 dxdy$$

$$+ \lambda_2 \cdot \int_{\text{outside}(C)} |f_0(x,y) - c_2|^2 dxdy, \qquad (1)$$

where $\mu \geq 0$, λ_1, $\lambda_2 > 0$ are fixed weight parameters, C is the evolving contour and length(C) is a regularizing term that prevents the final contour from converging to a small area due to noise, and c_1 and c_2 are mean values inside and outside of C, respectively. Note that many other active contour models are edge-based as opposed to the gray-level based method used here.

Equation (1) can be represented and solved by level set theory.[26] Level set theory, in which the two-dimensional evolving contour C is represented implicitly as the zero level set of a three-dimensional Lipschitz function $\phi(x,y)$, i.e., $C = \{(x,y) \in \Omega : \phi(x,y) = 0\}$, evolves the contour by updating the level set function $\phi(x,y)$ at fixed coordinates through iterations instead of tracking the contour itself. The initial level set function $\phi(x,y)$ is usually defined as the signed distance function:

$$\phi(x,y;t=0) = \pm d, \qquad (2)$$

where d is the distance from (x,y) to $C(t=0)$, where $C(t=0)$ corresponds to the initial contour. The plus (minus) sign is chosen if the point (x,y) is inside (outside) the initial contour $C(t=0)$.

With the evolution of the contour, the level set function ϕ cannot be held as a signed distance function, nor can it be kept smooth. In order to maintain a smooth level set function, and thus ensure numerical stability of evolution, it is necessary to reinitialize the evolving level set function to a signed distance function periodically. However, reinitialization is a computationally consuming procedure as it evolves solving the partial differential equation $\phi_t = \text{sign}(\phi_t)(1 - \|\nabla \phi_t\|)$, where $\nabla \phi_t$ corresponds to the gradient of the level set function. In addition, most reinitializing schemes tend to move the contour to some degree due to numerical errors.[27]

A signed distance function ϕ, however, has the intrinsic property that $\|\nabla \phi\| = 1$. Thus, it is more natural to incorporate this property into the contour evolution instead of using the independent reinitializing procedure previously described. Thus, we can introduce another regularizing term[28] in the active contour model in Eq. (1):

$$E(c_1, c_2, C) = \mu \cdot \text{length}(C) + \nu \cdot \frac{1}{2} \int_\Omega (1 - \|\nabla \phi_t\|)^2 dxdy$$

$$+ \lambda_1 \cdot \int_{\text{inside}(C)} |f_0(x,y) - c_1|^2 dxdy$$

$$+ \lambda_2 \cdot \int_{\text{outside}(C)} |f_0(x,y) - c_2|^2 dxdy, \qquad (3)$$

where ν is a weighted parameter and Ω represents the whole image space.

By replacing C with $\phi(x,y)$ in the energy functional in Eq. (3) and introducing the regularized versions of the Heaviside function $H_\epsilon(\phi) = \frac{1}{2}[1 + 2/\pi \arctan(\phi/\epsilon)]$ along with the corresponding Dirac measure $\delta_\epsilon(\phi) = d/d\phi H_\epsilon(\phi) = \epsilon \cdot [\pi \cdot (\epsilon^2 + \phi^2)]^{-1}$, as given by Chen and Vese in,[25] Eq. (3) can be expressed as:

$$E_\epsilon(c_1, c_2, \phi) = \mu \cdot \int_\Omega \delta_\epsilon(\phi(x,y)) \|\nabla \phi(x,y)\| dxdy$$

$$+ \nu \cdot \frac{1}{2} \int_\Omega (1 - \|\nabla \phi(x,y)\|)^2 dxdy$$

$$+ \lambda_1 \cdot \int_\Omega |f_0(x,y) - c_1|^2 H_\epsilon(\phi(x,y)) dxdy$$

$$+ \lambda_2 \cdot \int_\Omega |f_0(x,y)$$

$$- c_2|^2 \{1 - H_\epsilon[\phi(x,y)]\} dxdy, \qquad (4)$$

where the first integral controls the length of the contour and the second integral helps to smooth the level set function and thus avoid the need for reinitialization.

By fixing c_1 and c_2 and minimizing E_ϵ in terms of ϕ at each iteration, the associated Euler–Lagrange equation can be derived as:

$$\delta_\epsilon(\phi) \cdot [\mu \cdot \kappa - \lambda_1 \cdot (f_0 - c_1)^2 + \lambda_2 \cdot (f_0 - c_2)^2]$$

$$+ \nu \cdot \text{div}\left[\left(1 - \frac{1}{\|\nabla \phi\|}\right) \cdot \nabla \phi\right] = 0, \qquad (5)$$

where

$$\kappa = \text{div}\left(\frac{\nabla \phi}{\|\nabla \phi\|}\right) \qquad (6)$$

represents the curvature of the contour C, and also now incorporates the regularizing term from Li *et al.*[28] This derivation, combining the aspect of active contour without edges and level set without reinitialization, is given in the Appendix I. Using the gradient descent method, we can solve ϕ in Eq. (5) iteratively by letting ϕ be a function of iteration t and replace the zero on the right-hand side of Eq. (5) by the time derivative of ϕ. Thus, we obtain a partial differential equation as:

$$\frac{\partial \phi}{\partial t} = \delta_\epsilon(\phi) \cdot [\mu \cdot \kappa - \lambda_1 \cdot (f_0 - c_1)^2 + \lambda_2 \cdot (f_0 - c_2)^2]$$

$$+ \nu \cdot \text{div}\left[\left(1 - \frac{1}{\|\nabla \phi\|}\right) \cdot \nabla \phi\right]. \qquad (7)$$

The time derivative $\partial \phi / \partial t$ was approximated by a forward finite difference:

$$\frac{\delta \phi}{\delta t} = \frac{\phi^{n+1} - \phi^n}{\Delta t}, \qquad (8)$$

while considering the numerical stability of the PDE solution, the curvature κ was approximated by a discretizing

scheme that combines both forward and backward finite differences, as suggested in Ref. 29.

$$\kappa = \Delta_-^x \left(\frac{\Delta_+^x \phi_{i,j}^n}{((\Delta_+^x \phi_{i,j}^n)^2 + (m(\Delta_+^y \phi_{i,j}^n, \Delta_-^y \phi_{i,j}^n)^2)^{1/2}} \right)$$
$$+ \Delta_-^y \left(\frac{\Delta_+^y \phi_{i,j}^n}{((\Delta_+^y \phi_{i,j}^n)^2 + (m(\Delta_+^x \phi_{i,j}^n, \Delta_-^x \phi_{i,j}^n)^2)^{1/2}} \right), \qquad (9)$$

where

$$\Delta_\mp^x = \mp (\phi_{i\mp1,j} - \phi_{i,j}), \qquad (10)$$

and similarly for $\Delta_\mp^y \phi_{i,j}$;

$$m(a,b) = \left(\frac{sng(a) + sng(b)}{2} \right) min(|a|, |b|). \qquad (11)$$

III.B. Contour initialization

The energy function in Eq. (3) depends on the evolving curve C in a complex way. It is not guaranteed to be quadratic or even convex, and one might find a local minimum of the energy function somewhere in the neighborhood of the initial contour. Thus, initializing the contour is a nontrivial task for active contour models. Since lesion sizes vary, it is difficult to find fixed parameters (such as the radius of a circle) with which to initialize the contour for an entire database. Hence, we use our previous RGI-based segmentation method[7] to estimate the initial boundary of a lesion.

The RGI-based segmentation algorithm[7] incorporates prior knowledge that mass lesions are roughly compact, and thus, the original image $f(x,y)$ is multiplied with a two-dimensional constraint function $G(x,y;\mu_x,\mu_y,\sigma^2)$ to yield a preprocessed image $h(x,y)$ as

$$h(x,y) = f(x,y) \times G(x,y;\mu_x,\mu_y,\sigma^2), \qquad (12)$$

where $G(x,y;\mu_x,\mu_y,\sigma^2)$ is a Gaussian function centered at the manually indicated seed point (μ_x,μ_y), and with variance σ^2. The multiplication with the Gaussian function reduces the contribution of structures beyond the lesion, and thus, σ is set to 15 mm to accommodate most mammographic lesion sizes. We have found that the segmentation performance is not strongly dependent on the choice of σ. Larger lesions can also be segmented even though the small deviations around the margin of the lesion are usually not delineated well.

Starting from the given seed point (μ_x,μ_y), a series of gray level thresholds are then applied to the preprocessed image $h(x,y)$ to yield multiple contours. For each contour, an RGI value is calculated, where RGI is defined as

$$\text{RGI}(\mu_x,\mu_y,C_i) = \frac{\sum_{(x,y) \in C_i} \left(\nabla h(x,y) \cdot \frac{\hat{r}(x,y)}{\|\hat{r}(x,y)\|} \right)}{\sum_{(x,y) \in C_i} \|\nabla h(x,y)\|}, \qquad (13)$$

where C_i is the set of points on the ith contour, $\nabla h(x,y)$ is the gradient vector of $h(x,y)$ at point (x,y), and
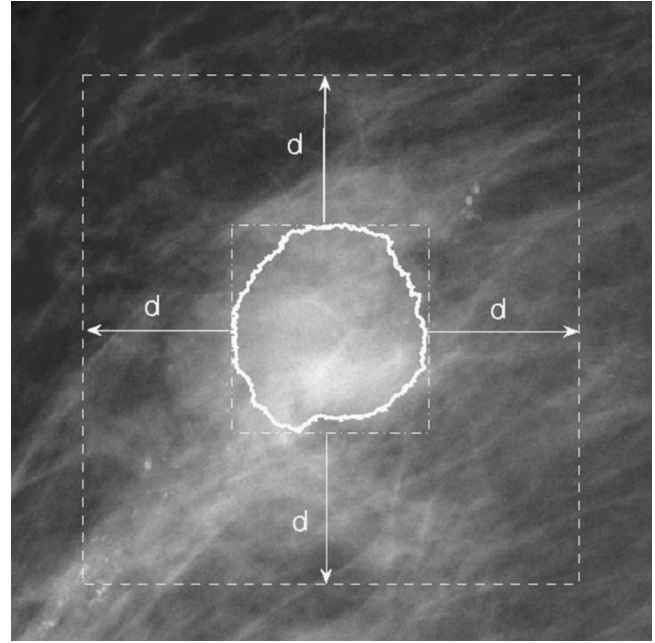

FIG. 3. Illustration of defining the effective background. In this figure, the solid line represents the initial contour obtained by RGI segmentation and the dashdotted rectangle is the circumscribed rectangle of this initial contour. The effective background is defined as the region inside the dashed rectangle excluding the region within the initial contour. An automatic scheme is employed to determine the best d.

$\hat{r}(x,y)/\|\hat{r}(x,y)\|$ is the normalized radial vector, the direction of which is calculated at position (x,y) with respect to the seed point (μ_x,μ_y). Of these contours, the one yielding the maximum RGI value is chosen as the contour that best delineates the lesion in the initial step.

RGI represents the average proportion of the gradients in the radially outward direction. The strategy of choosing maximum RGI works well for benign lesions as most have circularlike shapes and smooth margins. However, for malignant lesions, because of irregular shapes and spiculate margins, the resulting contours are usually undergrown. Nevertheless, RGI provides a good initial contour for the following evolution driven by active contour model.

III.C. Background estimation

In the active contour model, contour evolution relies on the competition between the region inside the contour (foreground) and that outside the contour (background). The presence of structure noises, such as lymph nodes, parenchyma, and localization markers, complicates the background in mammograms. RGI segmentation provides not only the initial contour, but also a means of estimating the effective background surrounding the lesion. In our study, the effective background is defined as the set of pixels within a given distance d (pixels) from the circumscribed rectangle of the initial contour, as shown in Fig. 3.

Distance d plays an important role in determining the effective background. On one hand, a large d yields a large
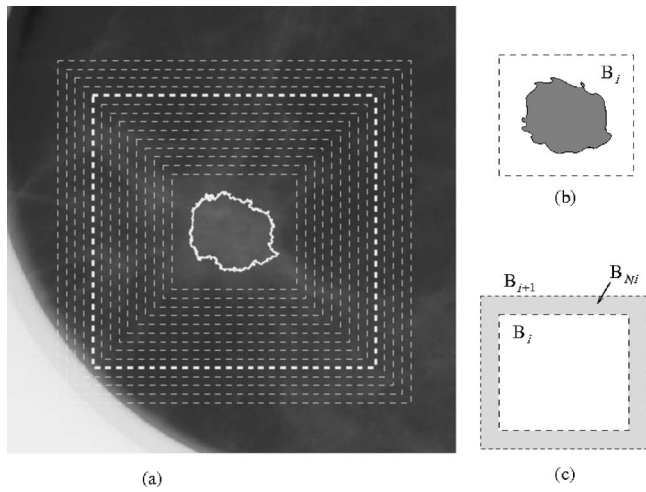
FIG. 4. The illustration of determining the distance d: (a) a mammogram with a series of distances d_i, in which the thick dashed rectangle represents the computer-selected distance d; (b) B_i: the ith background candidate corresponding to d_i; and (c) B_{Ni}: the ith net background increase. Background is defined as the set of pixels within a given distance d_i (pixel) from the circumscribed rectangle of the initial contour.

region and thus better statistics on the background. On the other hand, a small d would not be contaminated by nearby structures. In this study, an automatic scheme was developed to determine the best distance d from a series of candidates.

For a series of distances d_i, $i=1,\ldots,L$, two series of regions can be determined, as Fig. 4(a) shows. One series of regions are background candidates B_i [Fig. 4(b)], and the other series are net increases of background B_{Ni} [Fig. 4(c)], where $B_{Ni}=B_{i+1}-B_i$, $i=1,\ldots,L-1$. Our method is based on the following two principles: With the expansion of background, (1) the mean gray value of B_i, i.e., mean(B_i), should decrease as more areas with lower gray level are included and (2) the standard deviation of B_{Ni}, i.e., std(B_{Ni}), should not change substantially for relatively smooth background. By monitoring mean(B_i) and std(B_{Ni}) with increasing d_i, two

potential distance candidates are obtained. One candidate is defined as the distance at which mean(B_i) reaches a minimum value, and the other candidate is defined as the distance at which std(B_{Ni}) demonstrates the maximum increase, as shown in Fig. 5. At last, the final distance is chosen as the minimum of these two candidates. As for the example in Fig. 4, the distance is automatically determined $d=110$ (pixels).

III.D. Background trend correction

Due to the nonuniformity of the background distribution, some pixels in the background have similar gray values as in the lesion, which hinders the segmentation performance of the active contour model. Thus, a two-dimensional background trend correction was employed prior to segmentation. The background trend is estimated by fitting a two-dimensional surface with a least-squares method to the gradual change in the background pixel values within the extracted background estimation region. Here, we used a first-order polynomial function, i.e., $f(x,y)=a+b\cdot x+c\cdot y$, to describe the two-dimensional surface as higher order polynomial functions will estimate mass lesion instead. Figure 6 demonstrates the significance of the background trend correction when a nonuniform background is present.

III.E. Dynamic stopping criterion

To stop the evolution of a contour, a predetermined threshold is often used. Various metrics can be used to check convergence of evolution, such as the change of level set function ϕ[30] and the change of length of contour.[31] The contour evolution can also be terminated when the area inside the contour differs from the initial one by a given value.[32] In our initial study, we had defined a stopping criterion of relative foreground change (RFC), which is the ratio between the change of foreground and the area of foreground. Comparing with the stopping criterion of change of contour length used in,[31] RFC has two advantages: (1) RFC is a relative measure and thus is more suitable for lesions with various sizes and
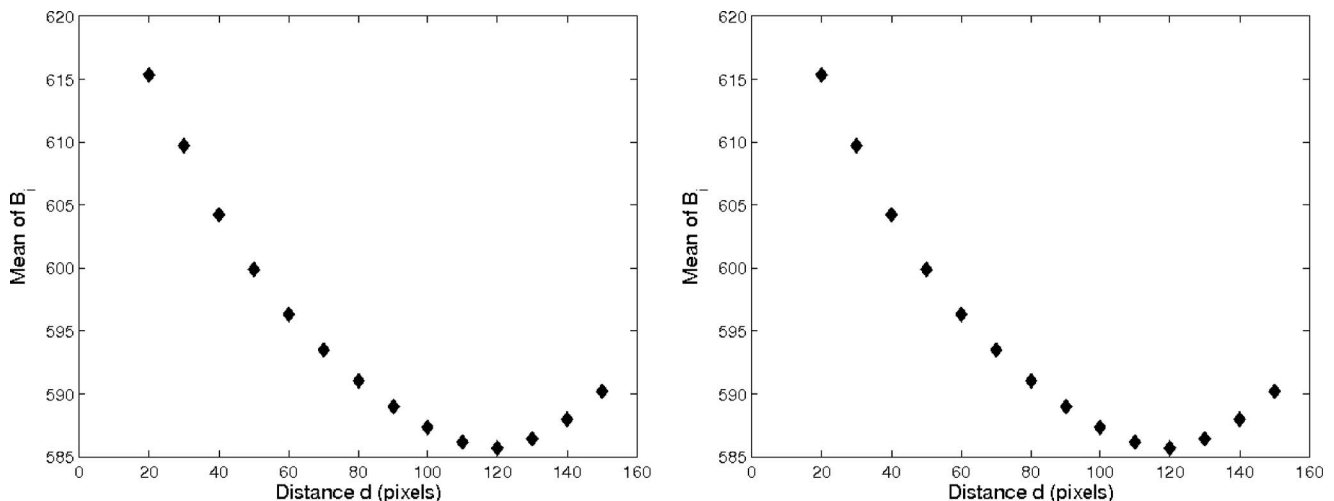

FIG. 5. Left: The trend of mean value of B_i, the ith background candidate with respect to distance d_i. Right: The trend of standard deviation of B_{Ni}, the ith net background increase with respect to B_i and B_{i+1}.
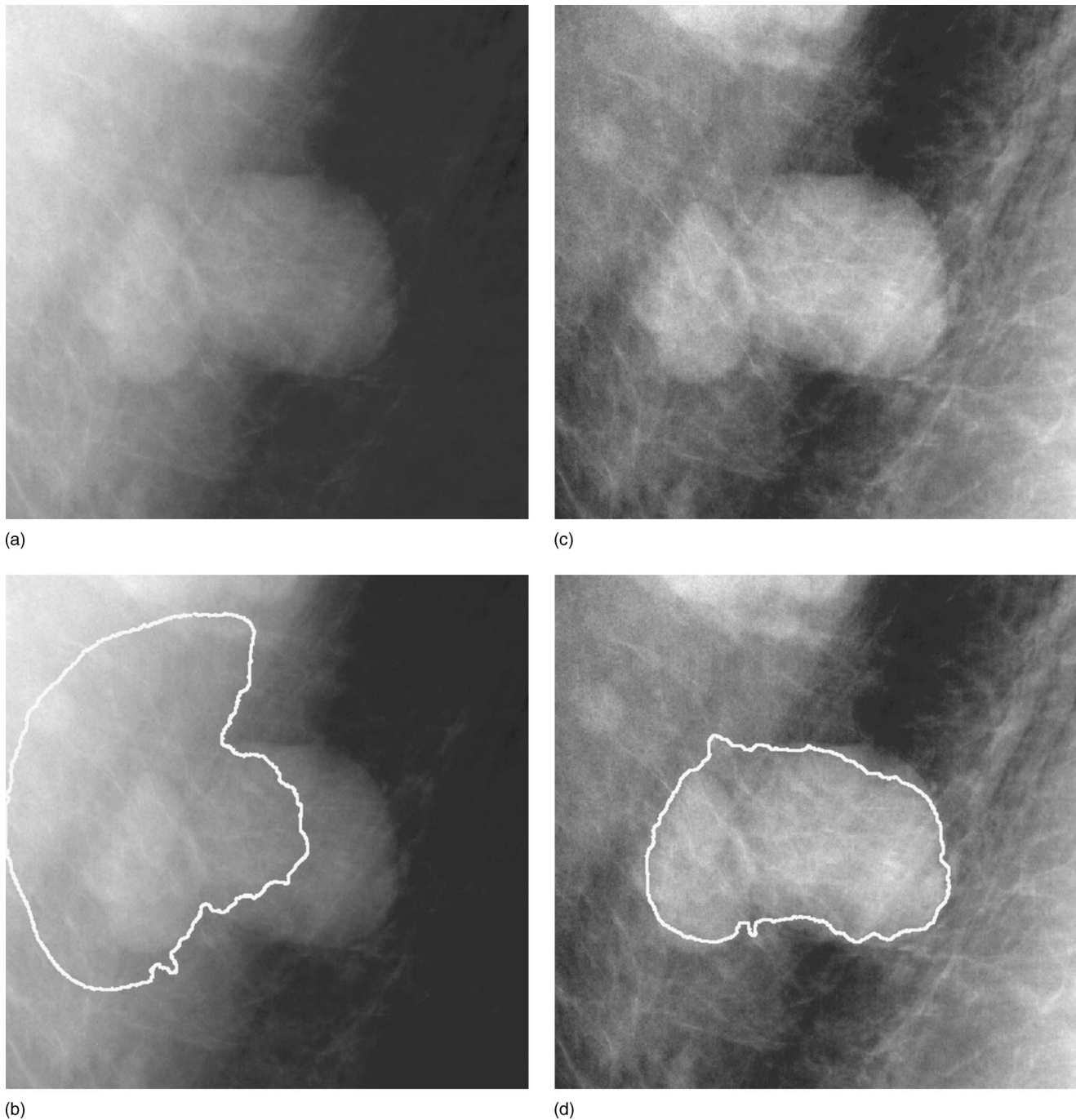
FIG. 6. An example of the effect of background trend correction on segmentation. (a) the original ROI; (b) segmentation result of (a); (c) the processed ROI after background trend correction; and (d) segmentation result of (c).

(2) RFC is more computationally efficient as the acquisition of contour in[31] brings additional computation. No matter what strategy is used, it is necessary to set some threshold in advance. However, due to varying sizes of lesions, as well as sizes of background obtained from automatic background estimation, it is difficult to find a fixed parameter for controlling convergence.

In our preliminary work,[33] we developed a dynamic method to terminate contour evolution automatically. In that work, as the contour evolves, the mean values of both foreground and background will decrease gradually. As the foreground is generally more homogeneous than the background, the rate of foreground mean change is less than that of background mean change. However, as the evolving contour crosses the lesion margin, the foreground mean will decrease faster than the background mean. Thus, during dynamic contouring, the difference between the rate of foreground mean change and that of background mean change is tracked, and contour evolution is terminated when the decrease of foreground mean value is more rapid than that of the background mean value. This method provides a way to terminate contour evolution free of predefined threshold. However, it ne-
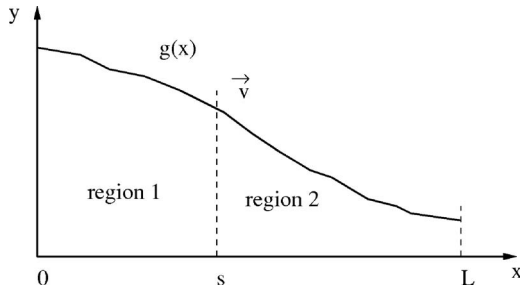
FIG. 7. The illustration of determining the stopping point. $g(x)$ is a decreasing function defined on $[0,L]$ and $s \in [0,L]$ is a moving point with speed of $\vec{v}$.

glects the influence of the sizes of both the foreground and background, and thus ceases contour evolution earlier than expected.

In order to address this problem, we modified the previous method, which we present here in one dimension. As Fig. 7 shows, $g(x)$ is a decreasing function defined on the interval $[0,L]$, and point s is moving within $[0,L]$ at the speed of $\vec{v}$. s also splits $[0,L]$ into two regions. For simplicity, the region $[0,s]$ is named region 1, and $[s,L]$ is region 2. Then, the mean values of regions 1 and 2 are:

$$c_1 = \frac{\int_0^s g(x)dx}{s}, \quad c_2 = \frac{\int_s^L g(x)dx}{L-s}.$$

The slope of c_1 is

$$\frac{dc_1}{dt} = \frac{dc_1}{ds} \cdot \frac{ds}{dt},$$

$$= \frac{d}{ds}\left(\frac{\int_0^s g(x)dx}{s}\right) \cdot \vec{v},$$

$$= \frac{g(s) - c_1}{s} \cdot \vec{v}.$$

Here, we use the fact that $\vec{v} = ds/dt \cdot \hat{v}$, where $\hat{v}$ is the outward unit vector. Similarly, the slope of c_2 is

$$\frac{dc_2}{dt} = \frac{g(s) - c_2}{L-s} \cdot \vec{v}.$$

Thus, the difference between these two slopes is

$$\Delta v = \frac{dc_1}{dt} - \frac{dc_2}{dt} = \left(\frac{g(s) - c_1}{s} + \frac{g(s) - c_2}{L-s}\right) \cdot \vec{v}. \quad (14)$$

As the discussed above, as s moves within the object, we have $\Delta v > 0$. As s moves across the edge, Δv will become negative. When $\Delta v = 0$, we have $g(s) = s/L \cdot c_2 + (L - s/L)c_1 > 1/2(c_1 + c_2)$, as in general $L - s > s$ and $c_1 > c_2$. However, if only the speed terms driven by image property in Eq. (7) are considered, the evolution should stop at s_0 such that $g(s_0) = 1/2(c_1 + c_2)$. Because of the influence of sizes, s will stop moving quickly if the criterion in Eq. (14) is used.

In order to eliminate the influence of size, a weighted difference between slope of c_1 and that of c_2 is introduced as

$$\Delta v_w = \frac{s}{L-s} \cdot \frac{dc_1}{dt} - \frac{dc_2}{dt} = \frac{1}{L-s} \cdot [2 \cdot g(s) - c(c_1 + c_2)] \cdot \vec{v}. \quad (15)$$

It can be shown that Δv_w goes to zero at the desired contour s_0, where $g(s_0) = 1/2(c_1 + c_2)$.

The one-dimensional case, described above, can be extended to a two-dimensional one. During the contour evolution, the weighted difference between the mean slope of foreground and that of background is monitored, and the contour evolution is terminated when the weighted slope difference converges to zero.

III.F. Implementation

In order to calibrate parameters in the proposed segmentation method, ten digitized screen-film mammograms (SFM) with spatial resolution of $100~\mu m \times 100~\mu m$ were analyzed. The calibrated segmentation method was then applied to the entire FFDM database for independent performance evaluation.

In our study, we kept both λ_1 and λ_2 in Eq. (7) to one (i.e., $\lambda_1 = \lambda_2 = 1$) since the contribution of the homogeneities of inside and outside the contour should be equally considered. Other parameters in Eq. (7) were chosen as follows: $\epsilon = 1$ and $\Delta t = 0.1$, where ϵ influences the Heaviside function and Δt controls how quickly the level set function changes. Note that μ controls the smoothness of the final contour. However, if one wants to depict the fine details of the object, one should choose a small μ. On the contrary, if one wants to obtain a smoother contour, one should set a large μ. As some of our computer-extracted features, such as spiculation, characterize the fine details of the lesion margin, we chose a fairly small value of μ, i.e., 0.001×1023^2, which also allows for the use of the 10-bit data. To ensure numerical stability, the coefficient v must satisfy $v \cdot \Delta t < 1/4$,[28] so we set $v = 2$ in our study. The maximum number of iterations is set to 500.

III.G. Performance evaluation

The performance of the proposed segmentation algorithm was assessed by comparing the computer-delineated contours with the outlines drawn by an expert breast radiologist. Besides visually evaluating the agreement of computer-segmented results with radiologist's manually contoured lesion margins, a quantitative measure was used to evaluate the segmentation performance. For a particular lesion, the area overlap ratio (AOR) between manual segmentation and computer segmentation is defined as

$$\text{AOR} = \frac{\text{Area}(M \cap C)}{\text{Area}(M \cup C)}, \quad (16)$$

where M is the manually segmented contour and C is the computer-segmented contour. AOR ranges from zero to one, with zero in the case of no overlap and 1.0 in the case of a perfect match. For the entire database, a series of AOR
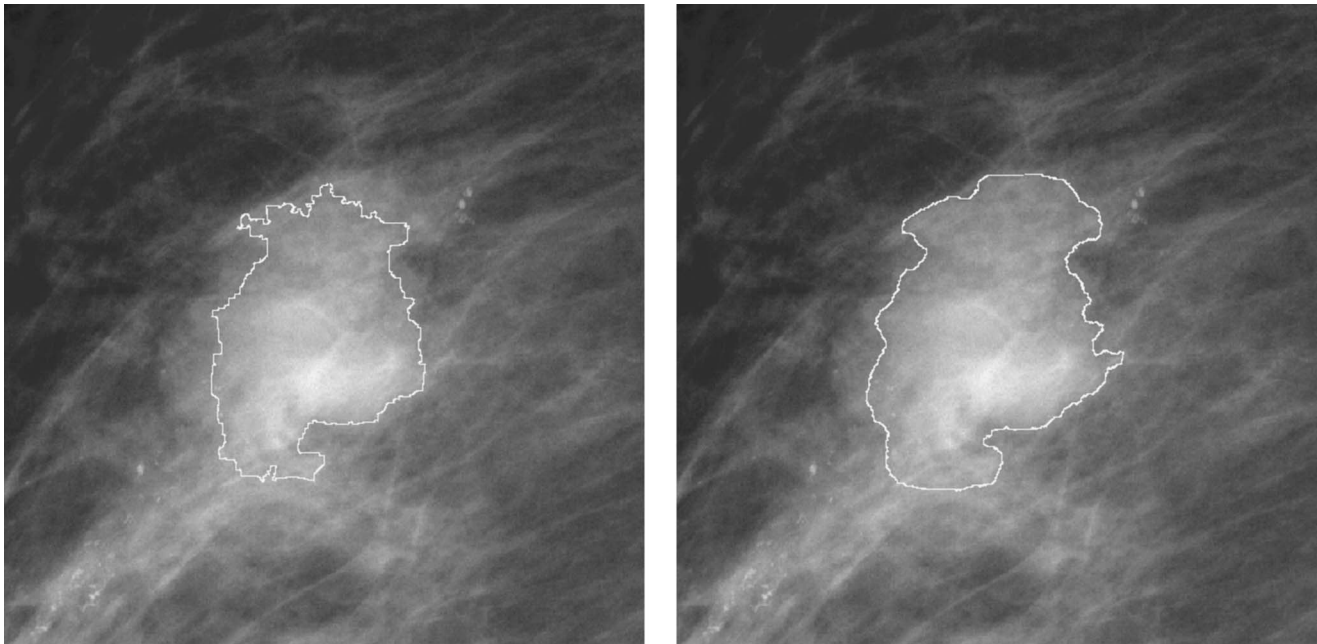
FIG. 8. An example of the effect of level set smoothness to the final segmentation results. Left: Segmentation without level set smoothness; Right: segmentation with level set smoothness.

thresholds were obtained and at each AOR threshold one the percentage of lesions "correctly" segmented was calculated by counting the number of lesions with AOR greater than that threshold.

IV. RESULTS

IV.A. Evaluation of level set smoothness

In our study, a new term $E_S \equiv \int_\Omega (1 - \|\nabla \phi_t\|) dx dy$ is added to the original active contour model in,[25] thus we initially evaluate the usefulness of this term. Two sets of final contours were extracted from the entire FFDM database; one was obtained with E_S and the other without. The results show that E_S cannot only provide a smoother contour, but also can push the contour closer to the lesion margin with less iterations, yielding a mean number of iterations of 160 compared to the mean number of iterations of 327 without E_S. In the example shown in Fig. 8, the left figure shows the segmentation result without smoothing level set function, which took 500 iterations. Meanwhile, for the result with smoothing level set function shown in the right figure, it took only 248 iterations to converge.

IV.B. Evaluation of dynamic stopping criterion

We investigated our new stopping criterion based on the weighted slope difference between foreground mean and background mean (Δv_w), and compared it to the unweighted slope difference method as well as the relative foreground change (RFC). The RFC thresholds to terminate contour evolution were set as 0.05, and 0.01, respectively. During the evolution, we recorded the contours using these four stopping criteria and obtained the AOR with radiologist's outlines.

Figure 9 shows plots of the fraction of correctly segmented lesions at various AOR threshold for the four stopping criteria (Δv_w, Δv, $\text{RFC}_{0.05}$, and $\text{RFC}_{0.01}$) on the FFDM databases. For benign images, all the criteria yielded similar segmentation performances since the initial contours, obtained by RGI segmentation, are close to the true lesion margins. However, as RGI segmentation is inferior for malignant lesions, Δv_w does perform better among all the stopping criteria.

Table I summarizes the statistical comparison (Holm t test)[34] among these four criteria, given the mean and standard deviation of AOR for each criterion. In terms of AOR, the weighted slope difference method is statistically better than the unweighted slope difference method, and the convergence rate at RFC=0.05 (overall significant level α^T =0.05). However, we failed to show a statistically significant difference between the weighted slope difference method and the convergence rate at RFC=0.01. Nevertheless, if the number of iterations is taken into account, the mean number of iterations for weighted slope difference is 156, while it is 280 for $\text{RFC}_{0.01}$. The weighted slope difference is more efficient than $\text{RFC}_{0.01}$.

IV.C. Comparative evaluation of the segmentation method

The segmentation algorithm was compared with our previously reported region-growing[6] and RGI-based segmentation[7] methods. Figure 10 shows several examples of lesion segmentations using these three segmentation methods. The result of the proposed method visually demonstrates a better agreement with the radiologist's outline of the lesion.

Figure 11 shows the fraction of lesions correctly segmented at various overlap threshold levels. At the overlap
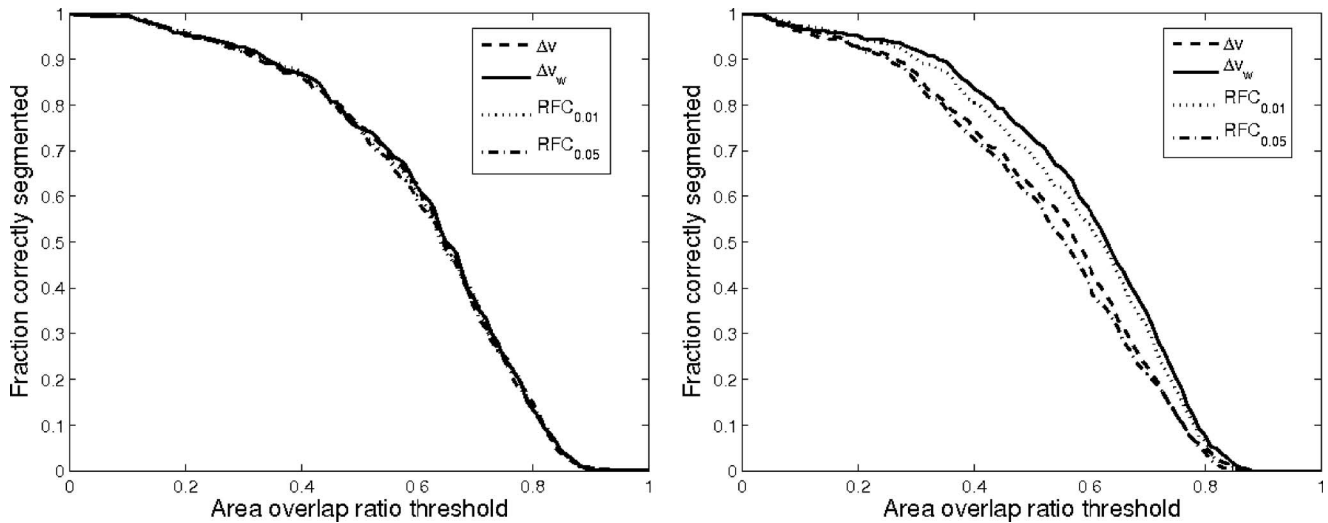
FIG. 9. Segmentation performance of four different stopping criteria in terms of AOR on a clinical FFDM database. In both plots, Δv_w is the weighted slope difference between foreground mean value and background mean value, in which foreground is the area within the evolving contour and background is the area outside contour; Δv is the unweighted slope difference between these two mean values. $RFC_{0.01}$ stands for a stopping criterion that terminates contour from evolution when the RFC is not greater than 0.01. Similarly, $RFC_{0.05}$ stops the contour evolution when RFC is not greater than 0.05. Left: evaluated on 327 benign images; Right: Evaluated on 412 malignant images. The results show that the weighted slope difference is statistically superior to unweighted slope difference and convergence rate at RFC=0.05 on malignant images.

threshold of 0.4, for benign lesions, 87% of the images are correctly segmented with the proposed method, while 72% and 81% of the images are correctly segmented by the region-growing and RGI-based methods, respectively. For malignant lesions, 84% of the images are correctly segmented with the proposed method, while 66% and 67% of the images are correctly segmented by region-growing and RGI-based methods, respectively.

Table II gives the statistical comparison (Holm *t* test)[34] for AOR means from the three segmentation methods. The improvement of AOR with the proposed method was found to be statistically significant (overall significant level $\alpha^T = 0.05$).

V. DISCUSSION

We developed a dual-stage segmentation method to efficiently segment mass lesions from the parenchymal surround in FFDM images. Our proposed method includes a geometric active contour model, which includes analysis of homogeneities both inside and outside of the evolving contour. The application of RGI-based segmentation to provide initial contour not only improves the computational efficiency, but also provides a method with which to estimate the effective background about the lesion and to suppress unrelated pixel

TABLE I. Statistical comparison of the performance of four stopping criteria in the dual-stage segmentation in terms of AOR, and *p*-values are given for the comparison of the weighted slope difference with any other stopping criterion. The significant level α_i for the individual paired *t* test is calculated using Holm's procedure (overall $\alpha^T = 0.05$). Same convention as Fig. 9.

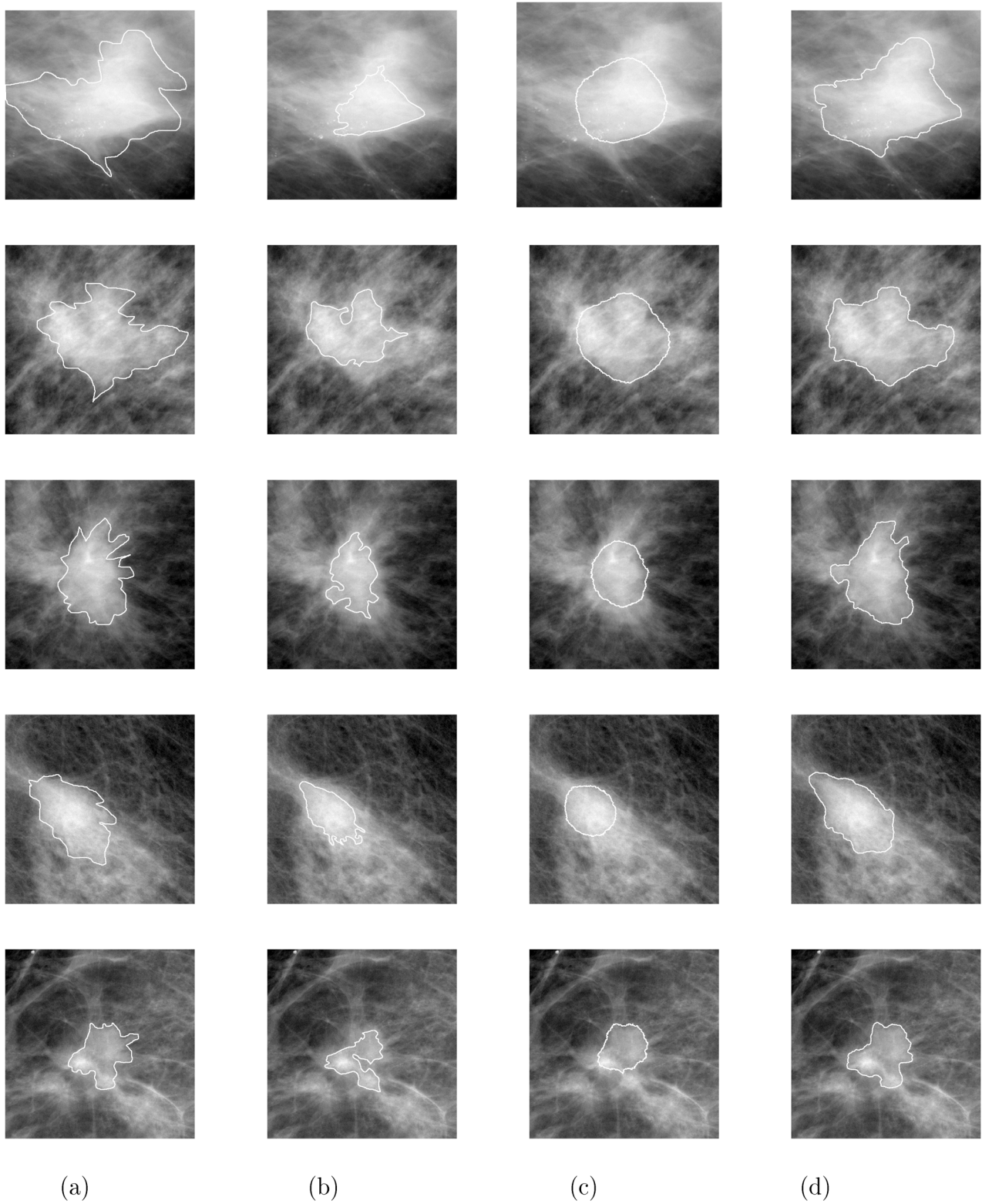|		Δv_w	Δv	$RFC_{0.01}$	$RFC_{0.05}$
Benign					
	mean±std	0.61±0.19	0.61±0.19	0.61±0.19	0.61±0.19
	p-value	—	0.856	0.801	0.601
	sig. lev. (α_i)	—	—	—	—
Malignant					
	mean±std	0.59±0.19	0.53±0.20	0.57±0.19	0.52±0.20
	p-value	—	<0.001	0.192	<0.001
	sig. lev. (α_i)	—	0.05	—	0.025
All					
	mean±std	0.60±0.19	0.57±0.20	0.59±0.19	0.56±0.20
	p-value	—	0.002	0.25	<0.001
	sig. lev. (α_i)	—	0.05	—	0.025

FIG. 10. Segmentation results for five malignant lesion examples: (a) radiologist's outline, (b) region-growing, (c) RGI-based segmentation, and (d) the proposed dual-stage segmentation method.
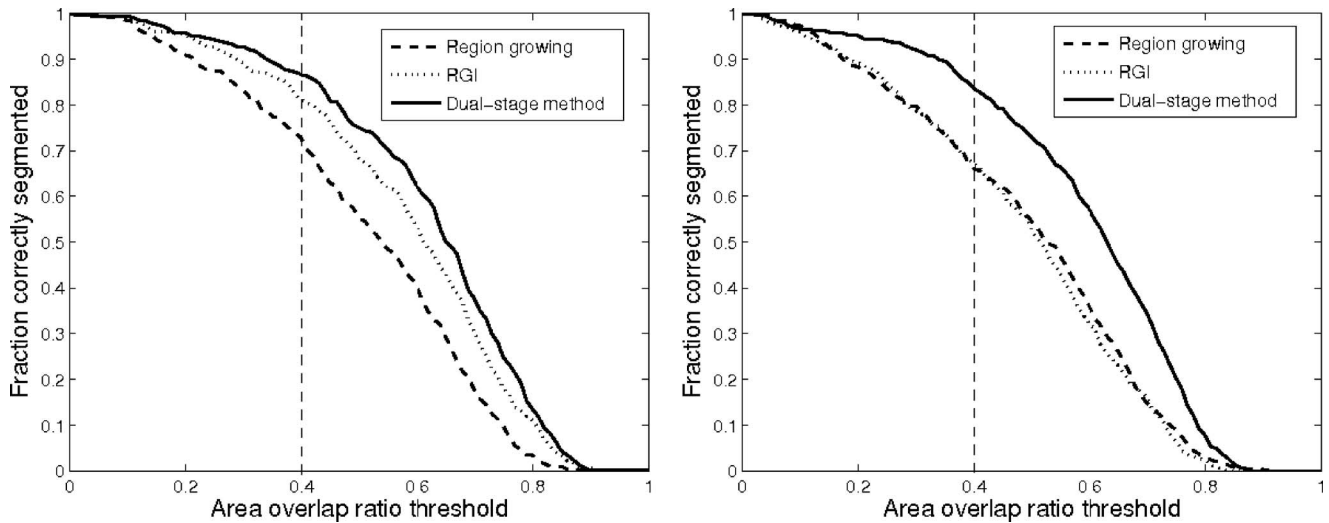
FIG. 11. Performance of three different segmentation methods in terms of AOR on a clinical FFDM database. Left: Evaluated on 327 benign images; Right: Evaluated on 412 malignant images. The results show that the dual-stage segmentation method is statistically superior to both region-growing and RGI-based method.

values. Also, our automatic stopping criterion is lesion-specific and does not rely on fixed iterations.

As the results show, the term E_S in the active contour model plays an important role in effective and efficient segmentation. As $\|\nabla\phi\| > 1$, $\mathrm{div}[(1-(1/\|\nabla\phi\|))\nabla\phi]$ will evolve the level set function ϕ toward reducing $\|\nabla\phi\|$, thus to smooth ϕ. The larger the gradient magnitude of level set function, the more it will be smoothed. While as $\|\nabla\phi\| < 1$, $\mathrm{div}\{[1-(1/\|\nabla\phi\|)]\nabla\phi\}$ will evolve the level set function toward increasing $\|\nabla\phi\|$ to maintain the gradient of the level set function to some level. This mechanism ensures the level set function, and thus the final contour, is relatively smooth. Meanwhile, as $\|\nabla\phi\|$ is restricted in magnitude, the foreground has the potential to grow faster.

It should be noticed that the weighted slope difference Δv_w is always non-negative as long as $g(x)$ is a decreasing

function. In the active contour model, if only the speed term driven by image property is considered, the speed of contour can be simplified as:

$$\vec{v} = [(g(s) - c_2)^2 - (g(s) - c_1)^2] \cdot \hat{v},$$

$$= (c_1 - c_2) \cdot [2 \cdot g(s) - (c_1 + c_2)] \cdot \hat{v},$$

where $\hat{v}$ is the outward unit vector. Inserting $\vec{v}$ into Eq. (15), we have:

$$\Delta v_w = \frac{1}{L - s} \cdot (c_1 - c_2) \cdot [2 \cdot g(s) - (c_1 + c_2)]^2 \cdot \hat{v} \geq 0.$$

If $\vec{v}$ is driven by another image property, such as edge information, this relationship still holds. When $g(s) > 1/2(c_1 + c_2)$, i.e., s is within the object, the contour will move outward to the edge, thus, we have $\Delta v_w \geq 0$. While if $g(s) < 1/2(c_1+c_2)$, i.e., s is out of object, it will move inward to the edge, we will also have $\Delta v_w \geq 0$. So the weighted slope difference also provides a general mechanism for terminating contour evolution with other active contour models.

In this study, we empirically compared the segmentation performance of the proposed method with our previously reported region growing[6] and RGI-based[7] segmentation methods. However, it is impossible for us to perform empirical comparisons between our method and those reviewed in the introduction section, as we do not have codes of those methods. Timp's method[10] uses polar coordinate and restricts the mass sizes within a certain range; thus one would expect their method to work better for lesions with circularlike margins. However, for lesions with irregular shapes or very large sizes, their method may have difficulty. Our dual stage segmentation method is able to handle this situation by further evolving the contour via the active contour model. For the fuzzy-set-based methods developed by Guliato *et al.*,[11] both of them need to present some thresholds such as the gray-level threshold in the first method and the maximum allowed

TABLE II. Statistical comparison of the three lesion segmentation algorithms. Performance is given by average AOR, and *p*-values are given for the comparison of the dual-stage segmentation with the previous region-growing and RGI-based method. The significant level α_i for the individual paired *t* test is calculated using Holm's procedure (overall $\alpha^T = 0.05$).

		Dual-stage segmentation	RGI	Region-growing
Benign				
	mean±std	0.61±0.19	0.58±0.19	0.51±0.20
	p-value	—	0.01	<0.001
	seg. lev. (α_i)	—	0.05	0.025
Malignant				
	mean±std	0.59±0.19	0.48±0.20	0.49±0.20
	p-value	—	<0.001	<0.001
	seg. lev. (α_i)	—	0.025	0.05
All				
	mean±std	0.60±0.19	0.52±0.20	0.50±0.20
	p-value	—	<0.001	<0.001
	seg. lev. (α_i)	—	0.05	0.025

difference between the value of the pixel being analyzed and the mean of the subregion in the second method, which prevents these methods from being applied in a large database. Their two thresholds were manually selected case by case in their evaluation using a database with 47 mammograms. On the other hand, our method is flexible in that no threshold needs to be set in advance.

In our preliminary study,[35] we compared two radiologists' outlines with a digitized screen-film mammograms (SFM) database, which consisted of 29 benign (51 mammograms) and 55 malignant (96 mammograms) lesions. At an overlap threshold of 0.4, 96.6% of lesion images were correctly segmented by one radiologist in comparison with the other. This result indicates that the radiologists highly agreed on the lesion margins for SFM. We could expect that the radiologists would also agree on the lesion margins for FFDM as the manufacturer has preprocessed the FFDM images to make them appear to the radiologist as traditional-looking SFM mammographs.

When we developed the proposed segmentation algorithm, the FFDM database was being constructed, so our method was initially calibrated and tested with the SFM database.[33] After building the FFDM database, we randomly picked three groups of FFDM images, each of which consisted of five benign and five malignant images, and evaluated the segmentation performance using the proposed method calibrated with SFM images. The results were similar with what we had obtained with SFM images. Thus, we believe that the parameters obtained by SFM also work with FFDM images, which was subsequently validated by the independent evaluation with the entire FFDM database.

Our results could be partially explained by the preprocessing of FFDM images, which is performed by the manufacturers. After preprocessing, the gray-level range and contrast of FFDM images become similar to those of SFM images, which ensures the possibility of applying parameters from SFM images to FFDM images as gray-level range and contrast are two key components used in our proposed lesion segmentation method. Our results also show the robustness of the proposed method as it mainly uses the global information of images.

VI. CONCLUSION

In this article, we present a new lesion segmentation method based on a geometric active contour model, which includes an initial RGI segmentation, background estimation, background trend correction, and a dynamic stopping criterion. Evaluation with a large number of FFDM images has shown that the proposed method is statistically superior to our previous region-growing and RGI-based algorithms in terms of overlap ratios obtained in comparison with experts' manual outlines. At an overlap threshold of 0.4, 85% of the images are correctly segmented by the proposed method, while only 69% and 73% of the images are correctly segmented by our previous region-growing and RGI-based methods, respectively.

APPENDIX

In this part, we provide the details of the derivation from energy function (4) to the associated Euler–Lagrange equation (5). For convenience, we restate Eq. (4) here as

$$E_\epsilon(c_1, c_2, \phi) = \int_\Omega \left[\mu \cdot \delta_\epsilon(\phi(x,y)) \| \nabla \phi(x,y) \| \right.$$
$$+ \frac{v}{2} \cdot (1 - \| \nabla \phi(x,y) \|)^2 + \lambda_1 \cdot |f_0(x,y)$$
$$- c_1|^2 H_\epsilon(\phi(x,y)) + \lambda_2 \cdot |f_0(x,y)$$
$$\left. - c_2|^2 (1 - H_\epsilon(\phi(x,y))) \right] dx dy. \tag{A1}$$

We define $F(\phi, \nabla \phi, x, y)$ as

$$F(\phi, \nabla \phi, x, y) = \mu \delta_\epsilon(\phi) \| \nabla \phi \| + \frac{v}{2}(1 - \| \nabla \phi \|)^2 + \lambda_1 |f_0$$
$$- c_1|^2 H_\epsilon(\phi) + \lambda_2 |f_0 - c_2|^2 (1 - H_\epsilon(0)). \tag{A2}$$

For simplicity, we have omitted the independent variables (x, y) of ϕ and f_0. According to calculus of variations, the scalar function $\phi(x, y)$ that minimizes $E_\epsilon(c_1, c_2, \phi)$ solves the PDE:

$$\frac{d}{dx}\left(\frac{\partial F}{\partial \phi_x} \right) + \frac{d}{dy}\left(\frac{\partial F}{\partial \phi_y} \right) - \frac{\partial F}{\partial \phi} = 0. \tag{A3}$$

Taking the partial derivative of F with respect to ϕ_x, ϕ_y, and ϕ, respectively, we have:

$$\frac{\partial F}{\partial \phi_x} = \mu \delta_\epsilon(\phi) \frac{\phi_x}{\| \nabla \phi \|} + v\left(\phi_x - \frac{\phi_x}{\| \nabla \phi \|} \right),$$

$$\frac{\partial F}{\partial \phi_y} = \mu \delta_\epsilon(\phi) \frac{\phi_y}{\| \nabla \phi \|} + v\left(\phi_y - \frac{\phi_y}{\| \nabla \phi \|} \right),$$

$$\frac{\partial F}{\partial \phi} = \mu \|\nabla \phi\| \delta'_\epsilon(\phi) + [\lambda_1(f_0 - c_1)^2 - \lambda_2(f_0 - c_2)^2]\delta_\epsilon(\phi),$$

(A4)

where $\delta'_\epsilon = d\delta/d\phi$ and we use the relation $\|\nabla\phi\| = \sqrt{\phi_x^2 + \phi_y^2}$.

The partial derivative of $\partial F/\partial\phi_x$ with respective to x is

$$\frac{d}{dx}\left(\frac{\partial F}{\partial\phi_x}\right) = \mu\delta'_\epsilon(\phi)\frac{\phi_x^2}{\|\nabla\phi\|} + \mu\delta_\epsilon(\phi)\frac{d}{dx}\left(\frac{\phi_x}{\|\nabla\phi\|}\right)$$
$$+ v\frac{d}{dx}\left[\phi_x - \frac{\phi_x}{\|\nabla\phi\|}\right].$$

(A5)

Similarly, we have

$$\frac{d}{dy}\left(\frac{\partial F}{\partial\phi_y}\right) = \mu\delta'_\epsilon(\phi)\frac{\phi_y^2}{\|\nabla\phi\|} + \mu\delta_\epsilon(\phi)\frac{d}{dy}\left(\frac{\phi_y}{\|\nabla\phi\|}\right)$$
$$+ v\frac{d}{dy}\left[\phi_y - \frac{\phi_y}{\|\nabla\phi\|}\right].$$

(A6)

Inserting Eqs. (A4)–(A6) back to (A3), we obtain

$$0 = \mu\delta'_\epsilon(\phi)\left[\frac{\phi_x^2}{\|\nabla\phi\|} + \frac{\phi_y^2}{\|\nabla\phi\|} - \|\nabla\phi\|\right] + \mu\delta_\epsilon(\phi)$$
$$\times\left[\frac{d}{dx}\left(\frac{\phi_x}{\|\nabla\phi\|}\right) + \frac{d}{dy}\left(\frac{\phi_y}{\|\nabla\phi\|}\right)\right] + v\left\{\frac{d}{dx}\left[\phi_x - \frac{\phi_x}{\|\nabla\phi\|}\right]\right.$$
$$+ \left.\frac{d}{dy}\left[\phi_y - \frac{\phi_y}{\|\nabla\phi\|}\right]\right\} - \delta_\epsilon(\phi)[\lambda_1(f_0 - c_1)^2$$
$$- \lambda_2(f_0 - c_2)^2].$$

(A7)

By noticing that

$$\frac{\phi_x^2}{\|\nabla\phi\|} + \frac{\phi_y^2}{\|\nabla\phi\|} = \|\nabla\phi\|,$$

$$\frac{d}{dx}\left(\frac{\phi_x}{\|\nabla\phi\|}\right) + \frac{d}{dy}\left(\frac{\phi_y}{\|\nabla\phi\|}\right) = \text{div}\left(\frac{\nabla\phi}{\|\nabla\phi\|}\right),$$

and

$$\frac{d}{dx}\left[\phi_x - \frac{\phi_x}{\|\nabla\phi\|}\right] + \frac{d}{dy}\left[\phi_y - \frac{\phi_y}{\|\nabla\phi\|}\right]$$
$$= \text{div}\left[\left(1 - \frac{1}{\|\nabla\phi\|}\right)\nabla\phi\right],$$

we finally obtain the compact form of Eq. (A7) as

$$0 = \delta_\epsilon(\phi)\left[\mu \cdot \text{div}\left(\frac{\nabla\phi}{\|\nabla\phi\|}\right) - \lambda_0(f_0 - c_1)^2 + \lambda_2(f_0 - c_2)^2\right]$$
$$+ v \cdot \text{div}\left[\left(1 - \frac{1}{\|\nabla\phi\|}\right)\nabla\phi\right].$$

(A8)

[a] Author to whom correspondence should be addressed. Electronic mail: yading@uchicago.edu

[1] A. J. Jemal, R. Siegel, E. Ward, T. Murray, J. Xu, and M. J. Thun, "Cancer statistics, 2007," Ca-Cancer J. Clin. **57**, 43–66 (2007).

[2] G. M. Newstead, "Role of MR in breast imaging," In *RSNA Categorical Course in Breast Imaging* (Chicago, 1999), pp. 287–293.

[3] S. G. Orel and M. D. Schnall, "MR imaging of the breast for the detec-tion, diagnosis, and staging of breast cancer," Radiology **220**, 13–30 (2001).

[4] A. T. Stavros, D. Thickman, C. L. Rapp, M. A. Dennis, S. H. Parker, and G. A. Sisney, "Solid breast nodules: Use of sonography to distinguish between benign and malignant lesions," Radiology **196**, 123–134 (1995).

[5] K. Horsch, M. L. Giger, L. A. Venta, and C. J. Vyborny, "Computerized diagnosis of breast lesions on ultrasound," Med. Phys. **29**, 157–164 (2002).

[6] Z. Huo, M. L. Giger, C. J. Vyborny, U. Bick, and P. Lu, "Analysis of speculation in the computerized classification of mammographic masses," Med. Phys. **22**, 1569–1579 (1995).

[7] M. A. Kupinski and M. L. Giger, "Automated seeded lesion segmentation on digital mammograms," IEEE Trans. Med. Imaging **17**, 510–517 (1998).

[8] N. Petrick, H. P. Chan, B. Sahiner, and M. A. Helvie, "Combined adap-tive enhancement and region-growing segmentation of breast masses on digitized mammograms," Med. Phys. **26**, 1642–1654 (1999).

[9] H. D. Li, M. Kallergi, L. P. Clarke, and V. K. Jain, "Markov random field for tumor detection in digital mammography," IEEE Trans. Med. Imaging **14**, 565–576 (1995).

[10] S. Timp and N. Karssemeijer, "A new 2D segmentation method based on dynamic programming applied to computer aided detection in mammog-raphy," Med. Phys. **31**, 958–971 (2004).

[11] D. Guliato, R. M. Rangayyan, W. A. Carnielli, J. A. Zuffo, and J. E. L. Desautels, "Segmentation of breast tumors in mammograms using fuzzy sets," J. Electron. Imaging **12**, 369–378 (2003).

[12] H. Li, Y. Wang, K. J. R. Liu, S. B. Lo, and M. T. Freedman, "Comput-erized radiographic mass detection—Part 1: Lesion site selection by mor-phological enhancement and contextual segmentation," IEEE Trans. Med. Imaging **20**, 289–301 (2001).

[13] M. Kass, A. Witkin, and D. Terzopoulos, "Snakes: Active contour mod-els," Int. J. Comput. Vis. **1**, 321–331 (1987).

[14] T. Cootes, A. Hill, C. Taylor, and J. Haslam, "The use of active shape models for locating structures in medical images," Image Vis. Comput. **12**, 355–366 (1994).

[15] M. S. Atkins and B. Mackiewich, "Fully automatic segmentation of the brain in MRI," IEEE Trans. Med. Imaging **17**, 98–107 (1998).

[16] A. Yezzi, S. Kichenassamy, A. Kumar, P. Olver, and A. Tannenbaum, "A geometric snake model for segmentation of medical imagery," IEEE Trans. Med. Imaging **16**, 199–209 (1997).

[17] C. Xu, D. L. Pham, and J. L. Prince, "Medical image segmentation using deformable models," in *Handbook of Medical Imaging: Medical Imaging Processing and Analysis*, edited by M. Sonka and M. J. Fitzpatrick (2000), vol. 2 of *Proc. SPIE*, pp. 129–174.

[18] J. Yang, L. H. Staib, and J. S. Duncan, "Neighbor-constrained segmenta-tion with level set based 3D deformable models," IEEE Trans. Med. Imaging **23**, 940–948 (2004).

[19] F. Liu, B. Zhao, and P. K. Kijewski, "Liver segmentation for CT images using GVF snake," Med. Phys. **32**, 3699–3706 (2005).

[20] G. M. Brake and N. Karssemeijer, "Segmentation of suspicious densities in digital mammograms," Med. Phys. **28**, 259–266 (2001).

[21] B. Sahiner, N. Petrick, H. P. Chan, L. M. Hadjiiski, C. Paramagul, M. A. Helvie, and M. N. Gurcan, "Computer-aided characterization of mammo-graphic masses: accuracy of mass segmentation and its effects on classi-fication," IEEE Trans. Med. Imaging **20**, 1275–1284 (2001).

[22] V. Caselles, R. Kimmel, and G. Sapiro, "Geodesic active contours," Int. J. Comput. Vis. **22**, 61–79 (1997).

[23] R. Malladi, J. A. Sethian, and B. C. Vemuri, "Shape modeling with front propagation: A level set approach," IEEE Trans. Pattern Anal. Mach. In-tell. **17**, 158–175 (1995).

[24] S. Osher and J. A. Sethian, "Fronts propagating with curvature-dependent speed: Algorithms based on Hamilton-Jacobi formulation," J. Comput. Phys. **79**, 12–49 (1988).

[25] T. F. Chan and L. A. Vese, "Active contours without edges," IEEE Trans. Image Process. **10**, 266–277 (2001).

[26] J. A. Sethian, *Level Set Methods and Fast Marching Methods: Evolving Interfaces in Computational Geometry, Fluid Mechanics, Computer Vi-sion, and Materials Science* (Cambridge University Press, Cambridge, 1999).

[27] S. J. Osher and R. P. Fedkiw, *Level Set Methods and Dynamic Implicit Surfaces* (Springer, New York, 2002).

[28] C. Li, C. Xu, C. Gui, and M. D. Fox, "Level set evolution without reini-tialization: A new variational formulation," In *Proc. 2005 IEEE CVPR*

(San Diego, 2005), pp. 1:430–436.

[29]L. Rudin, S. Osher, and E. Fatemi, "Nonlinear total variation based noise removal algorithms," J. Phys. D **60**, 259–268 (1992).

[30]R. Kimmel, *Numerical Geometry of Images: Theory, Algorithms, and Applications* (Springer, New York, 2003).

[31]K. N. Chaudhury and K. R. Ramakrishnan, "Stability and convergence of the level set method in computer vision," Pattern Recogn. Lett. **28**, 884–893 (2007).

[32]Y. Yu and J. A. Molloy, "Segmentation of the prostate from suprapubic ultrasound images," Med. Phys. **31**, 3474–3484 (2004).

[33]Y. Yuan, M. L. Giger, K. Suzuki, H. Li, and A. R. Jamieson, "A two-stage method for lesion segmentation on digital mammograms," in *Medical Imaging: Image processing*, edited by J. M. Reinhardt and J. P. W. Pluim (2006), vol. 6144 of *Proc. SPIE*, pp. 61443W:1–5.

[34]S. A. Glantz, *Primer of Biostatistics* (McGraw-Hill, New York, 2002).

[35]H. Li, M. L. Giger, Y. Yuan, L. Lan, K. Suzuki, A. R. Jamieson, and C. Sennett, "Comparison of computerized image analysis for digitized screen film mammograms and full field digital mammography images," in *Digital Mammography*, edited by S. M. Astley, M. Brady, C. Rose, and R. Zwiggelaar (2006), vol. LNCS4046 of *IWDM 2006*, pp. 569–575.